Chemical Engineering

DEM simulation of dry and wet granular material in a four-bladed mixer

Master's Thesis

Author:
Benedict Benque

Supervisor:
Prof. Johannes Khinast

September 22, 2016

Affidavit

I declare that I have authored this thesis independently, that I have not used other than the declared sources/resources, and that I have explicitly indicated all material which has been quoted either literally or by content from the sources used. The text document uploaded to TUGRAZonline is identical to the present master's thesis.

Ich erkläre an Eides statt, dass ich die vorliegende Arbeit selbstständig verfasst, andere als die angegebenen Quellen/Hilfsmittel nicht benutzt, und die den benutzten Quellen wörtlich und inhaltlich entnommenen Stellen als solche kenntlich gemacht habe. Das in TUGRAZonline hochgeladene Textdokument ist mit der vorliegenden Masterarbeit identisch.

_____   _____
Date   Signature

Abstract

The flow of dry and wet granular material in simple geometries cannot easily be predicted for design or optimization processes in its industrial applications. To better understand the granular behavior of a bed of monodisperse spherical beads in a four-bladed cylindrical mixer, the effect of various geometrical, operational and material parameters on the particle stress, mixing behavior and impeller torque were studied using DEM simulations.

The cohesive forces at different liquid contents were implemented using a simplified version of the model proposed by Mikami et al. [15], and the computational performance of the DEM simulation was enhanced by using reduced shear moduli.

In the observed range, the torque on the impeller and its fluctuation were proportional to the number of particles. The quasistatic regime was not observed at high fill heights in the dry simulations. The normal stress in the particle bed could be approximated by hydrostatics for the region above the blades. In the blade region, the stress was lower than predicted by hydrostatics.

The impeller torque decreased for higher blade clearances due to the lower shear rates below the blades. At a very low friction of $\mu_s = 0.1$, the particle bed moved almost as a solid block. At friction coefficients of 0.5 and 1.0, the particles moved slower and the torque increased. The particle movement was very similar for $\mu_s = 0.5$ and $\mu_s = 1.0$, both having a very high mixing rate compared to the low-friction case. Increasing the cohesiveness of the system also increased the torque and improved the initial mixing rate, but the mixing rate at high Bond numbers dropped severely after a few revolutions. The diffusion coefficient had its maximum at a Bond number of roughly ten.

Kurzfassung

Das Verhalten trockener und feuchter granularer Systeme in unkomplizierten Geometrien kann nicht auf einfache Weise vorhergesagt werden, wird jedoch in vielen industriell relevanten Auslegungs- und Optimierungsprozessen benötigt. Um das granulare Verhalten eines Betts monodisperser sphärischer Partikel in einem vierflügeligen zylindrischen Mischer besser zu verstehen, wurden in einer DEM-Simulation die Auswirkungen verschiedener Geometrie-, Betriebs- und Materialparameter auf die Spannungen, das Mischverhalten und das Drehmoment am Impeller untersucht.

Die Kohäsionskräfte bei verschiedenen Flüssigkeitsgehalten wurden mittels einer vereinfachten Version des Modells von Mikami et al. berechnet [15], und die Rechenperformance der DEM Simulation wurde durch eine Reduktion des Schubmoduls der Partikel verbessert.

Im untersuchten Bereich waren das Impellerdrehmoment sowie seine Fluktuation proportional zur Anzahl der Partikel. Bei Simulationen mit großen Füllhöhen konnte kein quasistatisches Regime beobachtet werden. Die Normalspannungen im Partikelbett über dem Impeller konnten durch hydrostatische Berechnungen angenähert werden. Im Bereich der Rührflügel waren die Spannungen jedoch geringer als die hydrostatische Näherung.

Das Drehmoment am Impeller nahm bei zunehmendem Abstand der Flügel vom Mischerboden ab, da bei größerem Abstand die Scherrate geringer war. Bei sehr geringer Reibung ($\mu_s = 0.1$) bewegte sich das Material als beinahe einheitliches Bett. Bei Reibungen von 0.5 und 1.0 bewegten sich die Partikel langsamer und das Drehmoment war höher. Die Partikel bewegten sich bei $\mu_s = 0.5$ und $\mu_s = 1.0$ auf sehr ähnliche Weise, und beide zeigten ein deutlich besseres Mischverhalten als die Simulationen bei geringer Reibung. Auch beim Erhöhen der Kohäsion stiegen das Drehmoment sowie die anfängliche Mischrate, jedoch sank die Mischrate nach wenigen Umdrehungen bei hohen Bondzahlen. Der Diffusionskoeffizient zeigte ein Maximum bei einer Bondzahl von etwa zehn.

Contents

1   Introduction

1.1   Motivation

The flow of dry and wet granular material, though relevant for numerous industrial branches such as the pharmaceutical and food industry, is not yet understood well enough to reliably predict its behavior. While fluid flows can be described using sets of first-principle equations with a known initial state and boundary conditions, no such tools are available for granular systems. Traditionally, heuristic methods are used for the design, scale-up and problem-solving of granular processes [17, p. 1ff].

While the behavior of granular flows in simple geometries such as shear flows or Couette flows has been studied extensively, less data is available on geometries commonly used in industrial processes. One of the most universally employed geometries is the cylindrical mixer agitated with an impeller. Although it is typically used to create homogeneous blends of granular material, it is in some cases used to improve the heat and mass transfer, e.g. in agitated drying [17, p. 3ff]. The flow patterns and shear rates as well as the influence of the geometry, the operating parameters and the particle properties in these agitated mixers have been studied by Brenda Remy [17].

1.2   Flow regimes

The rheological behavior of granular materials cannot be described as easily as that of fluid flows, since the correlation between stress and strain rates is not readily available [17, p. 4ff]. The local stress conditions determine whether a granular material behaves like an elastic solid or like a fluid. While in its elastic-solid state, it can support high loads. Since much of the load is distributed between the frictional bonds between the particles, the capacity is limited by these bonds [8].

Once enough bonds have been overcome, the granular material starts to flow in blocks consisting of many particles. These move along shear bands which approximately follow the stress characteristics of the material [8]. These shear bands are, however, not infinitesimally thin planes but rather zones with a depth in the order of ten particles. In these bands, the particles form force chains, i.e. structures that support the bulk of the stress [3]. As long as the movement is slow enough, the particles will stay in frictional contact with their neighbors. This regime is called quasistatic [8]. In this state, the bulk material can be considered a continuous plastic solid [3].

If, on the other hand, the speed is increased, the material will reach a state in which the particles move freely and without staying in contact with their initial neighbors. This is commonly called the rapid-flow regime. In this regime, the stress τ_{ij} correlates to the square of the shear rate γ, as demonstrated in equation 1. ρ_P is the particle density, R the particle radius, and f_{ij} is a tensor-valued function of the solid fraction v [8].

$$\tau_{ij} = \rho_{\mathrm{P}} R^2 f_{ij} \gamma^2 \tag{1}$$

The motion of a single particle in this regime can be described as the sum of the mean bulk velocity vector and a seemingly random velocity component. In analogy to the random thermal motion on a molecular level, the mean-square value of the random velocities is usually called granular temperature. Like the molecular temperature, the granular temperature generates pressure and governs the internal transport rates of mass, momentum, and energy. There are, however, fundamental differences between the molecular and the granular temperature. The granular temperature is lost almost instantaneously once no more energy is supplied to the system to make up for the energy lost in dissipation [8].

In an attempt to bridge the gap between the quasistatic and the rapid-flow regimes, Campbell [3, p. 219ff] proposed a model that considered the elastic properties of the material. He then divided the whole granular flow field into an elastic-quasistatic regime and an inertial regime. The former is governed by elastic forces while the latter is controlled mainly by inertial forces. In the transition regime (elastic-inertial), the forces are of the same order of magnitude. [3, p. 219ff]

In their study of the intermediate flow regime, Tardos et al. [25] suggested a dimensionless shear rate γ^* as shown in equation 2, wherein d_P is the particle size and g is the gravitational acceleration. The dimensionless shear rate was then used to describe different regimes of powder flow.

$$\gamma^* = \gamma \sqrt{\frac{d_p}{g}} \tag{2}$$

Their analysis of experimental data led to the conclusion that the torque and stress of a powder in an unconfined flow were independent of the shear rate. For confined Couette flows, however, he found that the dimensionless shear stress was dependent on $\gamma^{*\,n}$, wherein n appeared to be related to the particle concentration C. At very low shear rates - i.e., in the quasistatic regime - the index n was 0, effectively rendering the system independent of the shear rate.

At higher dimensionless shear rates (intermediate regime), Tardos et al. considered the correlation to be $\tau \propto (\gamma^*)^n$ with n starting below one and rising to one as the shear rate increased. At very high shear rates ($\gamma^* > 3$), the particle bed was in the rapid granular flow regime and followed $\tau \propto (\gamma^*)^2$.

The experimental data provided by Remy [17, p. 146ff] for bladed mixers showed the same shear-independent behavior for dimensionless shear rates $\gamma^* < 0.1$. It can be explained by the predominant mechanism for momentum transfer in the quasistatic regime, which is the formation of force chains. At low rotational speeds, the average number of these chains does not change for different speeds.

At higher shear rates ($\gamma^* > 0.1$), the shear stress scaled linearly with the shear rate [17, p. 146ff]. Extrapolating the stress to a shear rate of $\gamma^* = 0$ led to an offset of the stress, similar to the relation used to describe Bingham fluids: $\tau_{\sigma r} = \tau_y + \kappa \gamma^o$, with τ_y being the yield stress and κ the apparent viscosity [17, p. 147].

2

1.3   Cohesion

1.3.1   Regimes

Cohesive forces are attractive forces between the particles. Their origin may be van der Waals-forces, electrostatic charges, or capillary forces. For uncharged wet particles that exceed diameters of several hundred micrometers, the capillary forces caused by liquid bridges govern the cohesive behavior [1].

Different regimes can be described as the liquid content increases [16]:

Pendular: At low liquid contents, liquid bridges form between the particles. This results in capillary attraction. For spherical particles, the upper limit of this regime is a liquid volume fraction of 23 % [27].

Funicular: Some of the pores are completely filled with liquid while liquid bridges remain at some of the contact points. Both contribute to the capillary forces.

Capillary: All pores are completely filled with liquid. The liquid surface still forms menisci and the liquid pressure is lower than the ambient pressure. Capillary attraction exists.

Slurry/droplet: The particles are surrounded by liquid, the liquid surface is convex. The liquid pressure is equal to or higher than the ambient pressure. No capillary attraction exists.

Only the pendular regime was studied in this work.

1.3.2   Pressure and force in a liquid bridge

For the pendular case, the pressure difference from the ambient pressure P_a to the pressure in the liquid bridge P_l between two identical smooth spheres can be described by the Young-Laplace-equation (equation 3), where γ is the surface tension. This case is depicted in figure 1. The curvature term in parentheses in the Young-Laplace equation is positive when the meniscus is drawn back into the liquid, resulting in a liquid pressure that is lower than the ambient pressure [16].

$$\Delta P = P_a - P_l = \gamma \left(\frac{1}{r_1} + \frac{1}{r_2} \right) \tag{3}$$

As gravitation is a dominant force in many systems, the capillary force is often compared to gravity by calculating the capillary length a (see equation 4). For length scales much smaller than a, the capillary forces dominate the system. Length scales significantly larger than a occur in systems that are governed by gravitation [16].

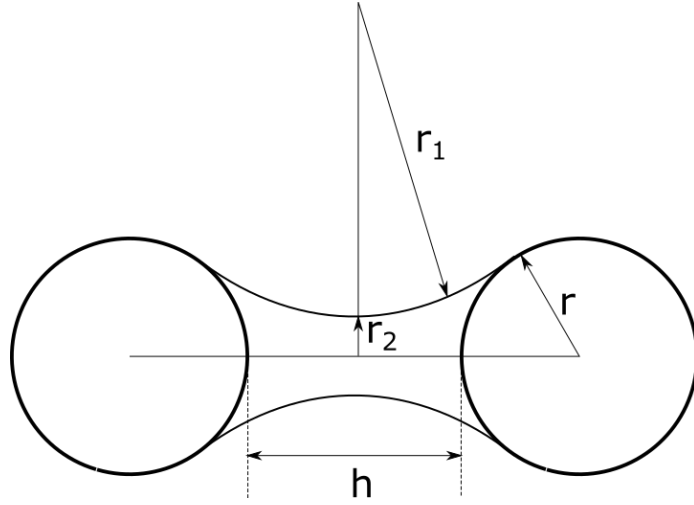$$a = \sqrt{\frac{2\gamma}{\rho_l g}} \tag{4}$$

Figure 1: Liquid bridge between two spheres

The attractive force between the two particles is the sum of the surface tension and the pressure difference, as shown in equation 5, where ΔP is given by equation 3.

$$F_{\text{bridge}} = 2\pi r_2 \gamma + \pi r_2^2 \Delta P \tag{5}$$

1.3.3   Bond number

The Bond number gives the ratio of the maximum cohesive force F_C to the gravitational force F_G (see equation 6). It can be described as a measure of the cohesiveness of the system [16].

$$Bo = \left| \frac{F_C}{F_G} \right| = \frac{2\pi R \gamma}{(4/3)\pi R^3 \rho g} = \frac{3\gamma}{2R^2 \rho g} \tag{6}$$

Li et al. [10] formulated a more extensive granular Bond number that includes the wetting angle θ. The index m stands for the smaller particles in non-homogenous particle beds.

$$Bo = \left| \frac{F_C}{F_G} \right| = \frac{2\pi R^* \gamma \left[cos(\theta) \right]_m}{(4/3)\pi g [R^3 \rho]_m} = \frac{3\gamma R^* \left[cos(\theta) \right]_m}{2g [R^3 \rho]_m} \tag{7}$$

At low shear rates, the Bond number indicates whether cohesion plays a significant role in the system [17].

1.3.4   Cohesion number

At high shear rates, the ratio of the maximum cohesive force to the average normal force becomes the relevant parameter. As can be seen in equation 8, the average normal force is the product of the pressure P in the system and

4

the square of the particle radius R. At values higher than one of this cohesion number η, cohesive forces play an important role in the system. [17][14].

$$\eta = \frac{N^c}{PR^2} \tag{8}$$

1.4 Rigid bed theory

The rigid bed theory describes the movement of the particle bed in a tank under the assumption that it moves like a solid cylindrical body at the blade rotational speed ω. The speed of a particle at the distance r from the center is

$$v = r\omega \tag{9}$$

Taking into consideration the shaft diameter leads to the following equation for the average speed of a particle in the bed:

$$|\bar{v}| = \frac{1}{(R_{\text{tank}}^2 - R_{\text{shaft}}^2)\pi} \int_{R_{\text{shaft}}}^{R_{\text{tank}}} (2\pi r)(\omega r) dr$$

$$|\bar{v}| = \frac{2}{3}\omega \left(\frac{R_{\text{tank}}^3 - R_{\text{shaft}}^3}{R_{\text{tank}}^2 - R_{\text{shaft}}^2} \right) \tag{10}$$

2 Methods

2.1 Discrete element method

The discrete element method (DEM) was used to describe the particulate system by integrating Newton's equations of motion beginning with the initial state. A sufficiently small time step was chosen for the simulation so that particles could be assumed to interact only with their neighbors. Therefore, only pairwise interactions of neighboring particles were taken into account to calculate each particle's position, velocity, and the resulting forces. The particle motion was then described by equations 11 and 12 [19].

$$m_i \frac{dv_i}{dt} = \sum_j (F_{ij}^N + F_{ij}^T) + m_i g \tag{11}$$

$$I_i \frac{d\omega_i}{dt} = \sum_j (R_i \times F_{ij}^T) + \tau_{rij} \tag{12}$$

These equations use the mass m_i, the radius R_i, the moment of inertia I_i, the velocity v_i, the angular velocity ω_i, and the gravitational acceleration g. The contact force was accounted for by equation 13, based on the work done by Tsuji et al. [26] [19].

$$F^N = -\tilde{k}_n \delta_n^{3/2} - \tilde{\gamma}_n \dot{\delta}_n \delta_n^{1/4} \tag{13}$$

In this equation, $\tilde{k}_n$ is the normal stiffness coefficient, δ_n is the normal displacement and $\tilde{\gamma}_n$ is the normal damping coefficient. The normal stiffness coefficient was calculated as follows:

$$\tilde{k}_n = \frac{E\sqrt{2R^*}}{3(1 - \nu^2)} \tag{14}$$

In this equation, E is the particle's Young modulus, which describes the response to uniaxial stress. It was calculated from the shear modulus G and the Poisson ratio ν as shown in equation 15 [12]. The effective radius R^* of the contacting particles was obtained from equation 16.

$$E = 2G(1 + \nu) \tag{15}$$

$$R^* = \frac{R_i R_j}{R_i + R_j} \tag{16}$$

Equation 17 yields the normal damping coefficient under the assumption of a constant coefficient of reconstitution e [21].

$$\tilde{\gamma}_n = -\frac{\ln e}{\sqrt{\ln^2 e + \pi^2}} \tag{17}$$

The other force needed to evaluate equations 11 and 12 is the tangential force, which was calculated from equation 18.

$$F^T = -\tilde{k}_t \delta_t - \tilde{\gamma}_t \dot{\delta}_t \delta^{1/4} \tag{18}$$

$\tilde{k}_t$ is the tangential stiffness coefficient, δ_t is the tangential displacement, and $\tilde{\gamma}_t$ is the tangential damping coefficient which was assumed to be equal to the normal damping coefficient. $\tilde{k}_t$ was calculated using the shear modulus G according to the work done my Mindlin [6]:

$$\tilde{k}_t = \frac{2\sqrt{2R^*G}}{2-\nu} \delta_n^{1/2} \tag{19}$$

The tangential displacement was obtained as follows:

$$\delta_t = \int v_{\mathrm{rel}}^t dt \tag{20}$$

The relative tangential velocity of the colliding particles resulted from the following equation.

$$v_{\mathrm{rel}} = (v_i - v_j) \cdot s + \omega_i R_i + \omega_j R_j \tag{21}$$

s denotes the tangential decomposition of the unit vector connecting the center of the particle.

The tangential force is limited by the Coulomb condition:

$$F^T < \mu_s |F^N| \tag{22}$$

In case the tangential force obtained from equation 18 was higher than the Coulomb limit, the tangential displacement was set to $\delta_t = {}^{F^T}/k_t$ [19].

2.2 Cohesion model

The DEM simulation needed an explicit calculation of the liquid bridge force F_{bridge} from the particle radius R, the liquid volume V, the surface tension γ, the contact angle β, and the separation distance h. Also, the rupture distance h_{rupture} and the viscous resistance F_{viscous} needed to be calculated [16]. The relation used in the simulations was proposed by Mikami et al. [15].

It calculated the liquid bridge force between particles from a regression expression based on numerical simulations of the Young-Laplace equation (equation 3).

A normalized capillary force $\hat{F}^c$ was defined as

$$\hat{F}^c = \frac{F^c}{2\pi R\gamma} \tag{23}$$

where γ is the surface tension. The expression for the calculation of $\hat{F}^c$ was

$$\hat{F}^c = exp(A\hat{h} + B) + C \tag{24}$$

The parameters A, B and C for particle-particle interactions were calculated as follows:

$$A = -1.1\hat{V}^{-0.53} \tag{25}$$

$$B = (-0.34\ln(\hat{V} - 0.96)\theta^2 - 0.019\ln\hat{V} + 0.48 \tag{26}$$

$$C = 0.0042\ln\hat{V} + 0.0078 \tag{27}$$

For particle-wall-interactions, the following equations were used [23]:

$$A = -1.9\hat{V}^{-0.51} \tag{28}$$

$$B = (-0.016\ln(\hat{V} - 0.976)\theta^2 - 0.012\ln\hat{V} + 1.2 \tag{29}$$

$$C = 0.013\ln\hat{V} + 0.18 \tag{30}$$

θ is the contact angle of the liquid bridge. The dimensionless liquid bridge volume is

$$\hat{V} = \frac{V}{R^3} \tag{31}$$

and the dimensionless separation distance between the particle surfaces is

$$\hat{h} = \frac{h}{R} \tag{32}$$

The distance at which the pendular bridge broke was determined according to an equation by Lian et. al. [11].

$$\hat{h}_c = R^*(0.62\theta + 0.99)\hat{V}^{0.34} \tag{33}$$

The influence of the viscosity can be described by the Capillary number [20]:

$$Ca = \frac{\eta U}{\gamma} \tag{34}$$

η is the dynamic viscosity of the liquid and U is the characteristic speed. At the highest rotational speed used in the simulations (200 rpm), the tip speed was $0.94\,\mathrm{m\,s^{-1}}$. For a granular system with water at $20\,°\mathrm{C}$, the resulting capillary number was 0.013. Since the viscous forces appeared to be very small compared to the capillary forces, they were neglected in the simulations.

Furthermore, the cohesive forces were assumed to only apply as long as the particles were in physical contact. This simplification avoided the high computational demands of considering forces between particles that were up to the rupture distance apart from each other.

2.3 Stiffness modification to reduce the computational time

The Rayleigh time step is the time needed by a shear wave to propagate through a particle, and is therefore the maximum time step for a quasistatic DEM simulation. Equation 35 shows how the Rayleigh time step was evaluated by EDEM. R is the radius of the biggest particle, ρ is the particle density, G stands for the shear modulus, and ν is the Poisson's ratio [22].

$$T_{\mathrm{R}} = \frac{\pi R \sqrt{\rho/G}}{0.1631\nu + 0.8766} \tag{35}$$

For systems that are not in the quasistatic regime, time steps of around $0.2T_{\mathrm{R}}$ (at coordination numbers ≥ 4) to $0.4T_{\mathrm{R}}$ (at low coordination numbers) are recommended by the EDEM documentation [22].

As T_{R} scales with $1/\sqrt{G}$, the time step increases for lower values of the shear modulus [22].

The Hertz-Mindlin model implemented in EDEM calculated the normal contact forces F_n according to equation 36. k_{HM} is the normal stiffness, δ_n the normal overlap, c_{HM} the normal damping coefficient (a function of the coefficient of restitution e), v_n is the normal relative velocity, and $\vec{n}$ is the unit vector from the center of the colliding particle [12].

$$\vec{F}_n = \vec{F}_{n,k} + \vec{F}_{n,d} = \left(k_{\mathrm{HM}} \delta_n^{3/2} + c_{\mathrm{HM}} \vec{v}_n \delta_n^{1/4} \vec{n} \right) \vec{n} \tag{36}$$

The stiffness k_{HM} was calculated as follows:

$$k_{\mathrm{HM}} = \frac{4}{3} E^* \sqrt{R^*} \tag{37}$$

The effective radius R^* of the particles was calculated as shown in equation 16. The effective Young's modulus E^* follows equation 38, wherein ν is the Poisson's ratio.

$$\frac{1}{E^*} = \frac{1 - \nu_i^2}{E_i} + \frac{1 - \nu_j^2}{E_j} \tag{38}$$

A reduction of the shear modulus G leads to a reduction of the Young's modulus, as can be seen in equation 15, and of the stiffness k_{HM}. Since the Rayleigh time step scales with $1/\sqrt{G}$, the lower stiffness then allows for larger time steps in the simulation, thus reducing the computational time. No general recommendation can be given for the value of G [12]. Instead, the momentum of the colliding particles has to be taken into account. Therefore, a comparison of the normal overlap instead of the shear modulus was suggested [12].

A study conducted by Malone and Xu [13] suggested that even for the normal overlap, no general limit can be stated. The amount of overlap that can be permitted without significantly changing the behavior depends on the system and on which variables are of interest. Typical values for reported acceptable overlaps lie in the range of $0.1\,\%$ to $1\,\%$. In the case of cohesive systems, low

values for the stiffness lead to defluidization, whereas a high contact stiffness results in smooth fluidisation [13].

For a system similar to the geometry 1 described in appendix A.1, Brenda Remy [19] allowed the maximum normal overlap to reach $4\,\%$, with an average normal overlap of $< 1\%$.

2.3.1 EDEM simulation of two-particle collisions

The normal overlap was observed in simple EDEM simulations of one particle moving at speed v_{col} colliding with a stationary particle.

The effect of the time step on the resolution (i.e. the amount of time steps per collision) was studied at different values for the shear modulus and at various collision velocities. The collision speeds were varied from $0.12\,\mathrm{m\,s^{-1}}$ to $0.96\,\mathrm{m\,s^{-1}}$. Since no fully elastic collisions were allowed to occur in the stirred tank simulations, this assumption was an overestimation.

The reference speed for particles in the stirred tank simulations was the impeller tip speed v_{tip}. In both geometry 1 and geometry 2, the investigated collision speed range of $0.12\,\mathrm{m\,s^{-1}}$ to $0.96\,\mathrm{m\,s^{-1}}$ corresponded to an rpm range of 12.5 rpm to 100 rpm. To achieve a good resolution of the collisions, a minimum amount of 20 time steps per collision was assumed to be necessary. A low resolution (few time steps per collision) led to high overlaps and, subsequently, high normal forces and accelerations. These caused exit speeds that were significantly higher than the ones suggested by the coefficient of restitution, and in some cases even surpassed the collision speed.

The amount of time steps for each collision was approximately inversely proportional to the relative time step under the studied conditions (see figure 2).

Therefore, the necessary relative time step to fulfill the resolution criterion could easily be estimated from the two-particle simulations at different speeds and shear moduli. It is shown in figure 3, which is valid for particle diameters of $2\,\mathrm{mm}$ and $3\,\mathrm{mm}$. For a simulation that needed to be conducted at a given shear modulus and rotational speed, the tip speed was calculated from the geometry. The maximum allowed percentage of the Rayleigh time step that still resulted in a resolution of at least 20 time steps per collision could be read at the intersection of the shear modulus with the line for the collision speed.

2.3.2 Choosing the shear modulus from the settling behavior and the impeller torque

EDEM simulations were conducted to determine the lower limit of the shear modulus to still be able to depict the system without significant deviation from the expected height of the particle bed. A given amount of particles was allowed to settle without any blade rotation in the geometry 1. The steady-state values for the overlap as well as the filling height were observed at different values for the shear modulus G. As shown in figure 4, the bed height is low at low shear moduli and levels off at a shear modulus of the order of magnitude $3 \times 10^6\,\mathrm{Pa}$. This suggested that any shear modulus above that value was able to depict the system without a significant error in the bed height.
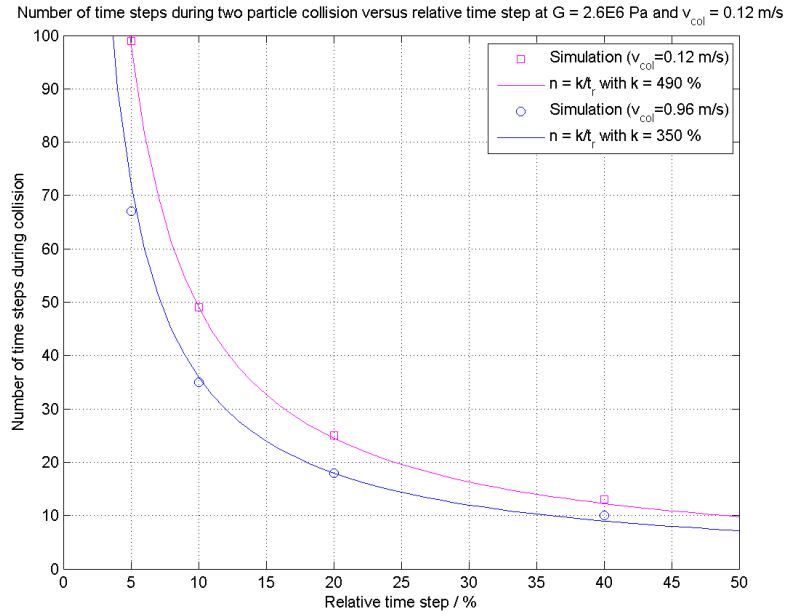
Figure 2: Number of time steps during two-particle collision versus relative time step
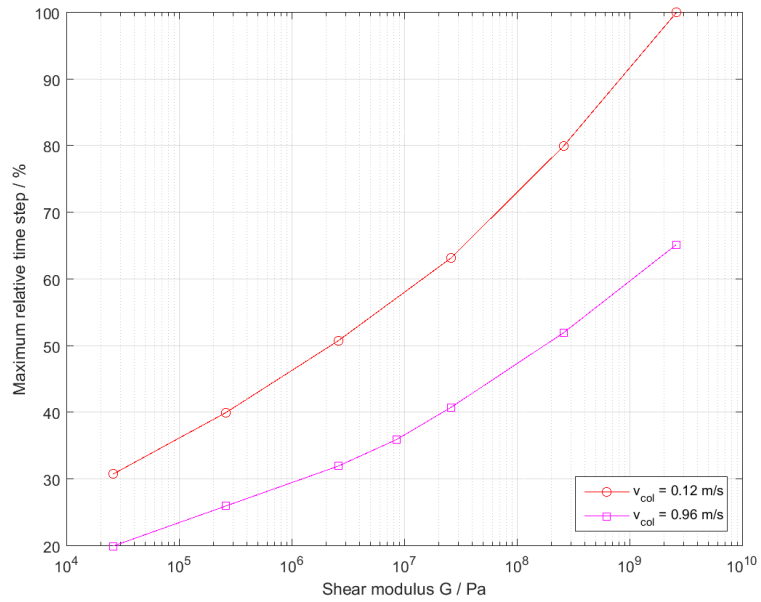

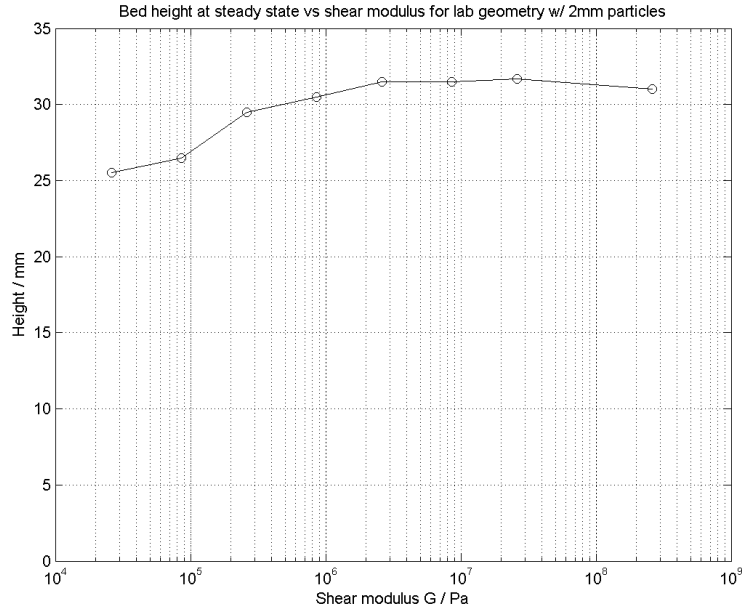Figure 3: Necessary relative time step for the two-particle collision

Figure 4: Height of the particle bed in the geometry 1 for different shear moduli

The torque on the impeller at different shear moduli in the range of $2.6 \times 10^4 \, \mathrm{Pa}$ to $8.6 \times 10^8 \, \mathrm{Pa}$ was also observed at a rotational speed of 50 rpm and a friction of $\mu_s = 0.1$. The torque increased with higher shear moduli until leveling off at a shear modulus of roughly $1 \times 10^7 \, \mathrm{Pa}$.

2.3.3 Effect of the shear modulus on the speed profile

In the geometry 1 at a blade clearance of 5 mm and a fill level that just covered the blade, the particle bed was stirred at 50 rpm. The static friction was set to $\mu_s = 0.1$. The speed profile was studied for different shear moduli in the range of $2.6 \times 10^4 \, \mathrm{Pa}$ to $2.6 \times 10^8 \, \mathrm{Pa}$. The results are shown in figure 5.

It was observed that lower shear moduli led to the particle bed behaving more like a rigid bed. This could be traced to the longer collision times and lower collision frequency for softer particles. They tended to stay in contact longer during a collision, whereas stiffer particles had more collisions per time interval due to the small overlaps and the resulting short contact times.

2.3.4 Effect of the stiffness on the collision speed and number of collisions

A dimensionless normal collision speed was defined as

$$v_n^* = \frac{v_n}{\omega R_{\mathrm{blade}}} \tag{39}$$

13
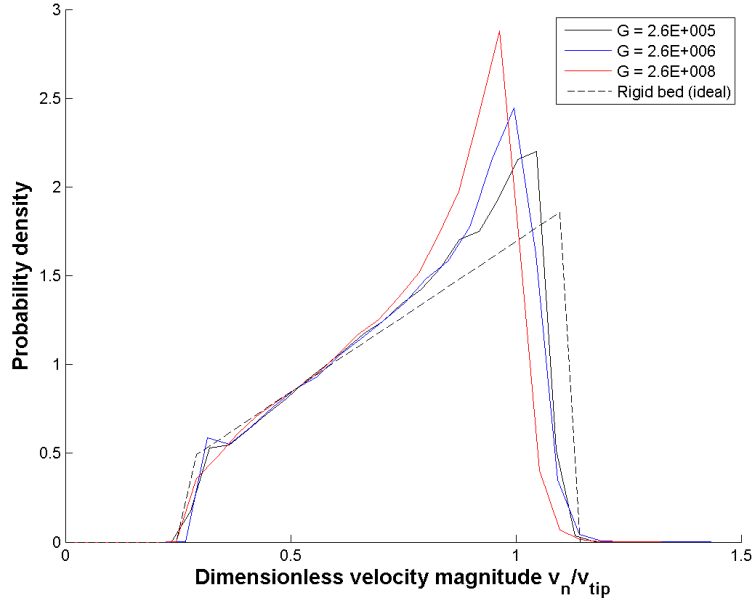
Figure 5: Speed profile in the geometry 1 mixer at 50 rpm for different shear moduli G ($\mu_s = 0.1$)

where ω was the rotational speed and R_{blade} was the blade radius.

The cumulative distribution of the dimensionless normal collision speed was studied for simulations of glass beads at a fill level that just covered the blades in the geometry 1 at a rotational speed of 50 rpm and with a static friction of $\mu_s = 0.1$. The results for different shear moduli G can be seen in figure 6. At high shear moduli, the distribution moved towards low collision speeds.

The number of collisions rose as the particles became stiffer. This might be traced back to the lower overlap and the resulting short contact times for stiff particles. Softer particles, on the other hand, tend to remain in contact for a long time, resulting in a lower number of contacts in the same time span.

2.3.5 Monitoring of the normal overlap

For all simulations within the scope of this work, the maximum and the average value for the normal overlap were documented. The maximum overlap was sensitive to the simulated time span while the average normal overlap provided a more robust tool for the comparison of simulations.

The average overlap δ_{avg} showed a linear dependence of the simulation time step t_{sim}. The correlation to the shear modulus G and the impeller speed ω could be described by a power law:

$$\delta_{\text{avg}} = a \cdot f(G) + b \cdot G^c \cdot \omega \cdot t_{\text{sim}} \tag{40}$$

14
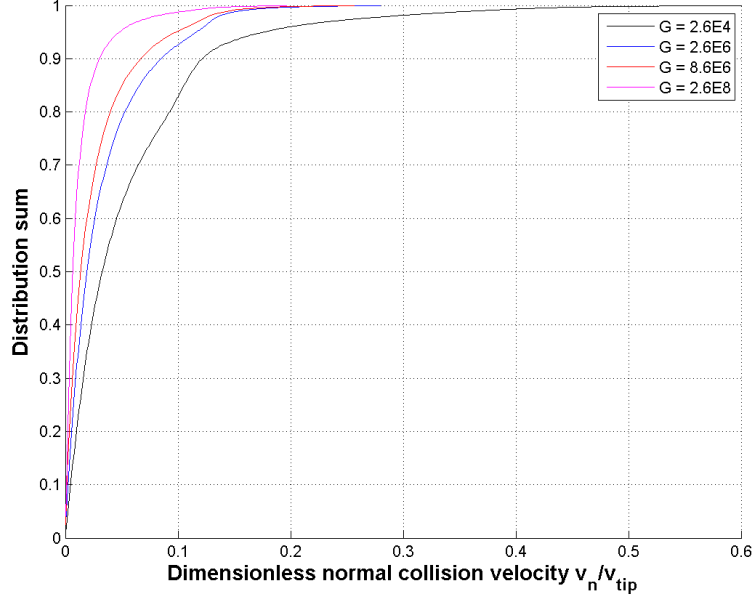
Figure 6: Cumulative distribution of the normal collision speed at different shear moduli

The shear modulus was, however, set to the same value ($G = 8.6 \times 10^6$ Pa) for most simulations and equation 40 was simplified to:

$$\delta_{\mathrm{avg}} = a' + b' \cdot \omega \cdot t_{\mathrm{sim}} \tag{41}$$

For simulations in both geometries, the sensitivity of the overlap to the fill height of the tank was analyzed. In the quasistatic regime, the average normal overlap rose almost linearly with the fill height in the observed H/D (fill height to tank diameter) range of 0.32 to 1.30 (see figure 7). In the intermediate regime, the sensitivity of the dry simulation to the bed height diverged from the linear behavior, whereas the overlap in the wet simulations responded linearly to the fill height (see figure 8). This suggests that for a dry bed in the intermediate regime, the average overlap was dominated by shear forces for low fill heights and by the weight of the particle bed at high levels.

2.4 Bulk density

The bulk density was calculated for different height elements from the number N of particles in that height element and the volume V_{he} of each height element under consideration of the volume taken up by the shaft and blades:

$$\rho_{\mathrm{bulk}} = \frac{N d_p^3 (\pi/6) \rho_p}{V_{he}} \tag{42}$$

15
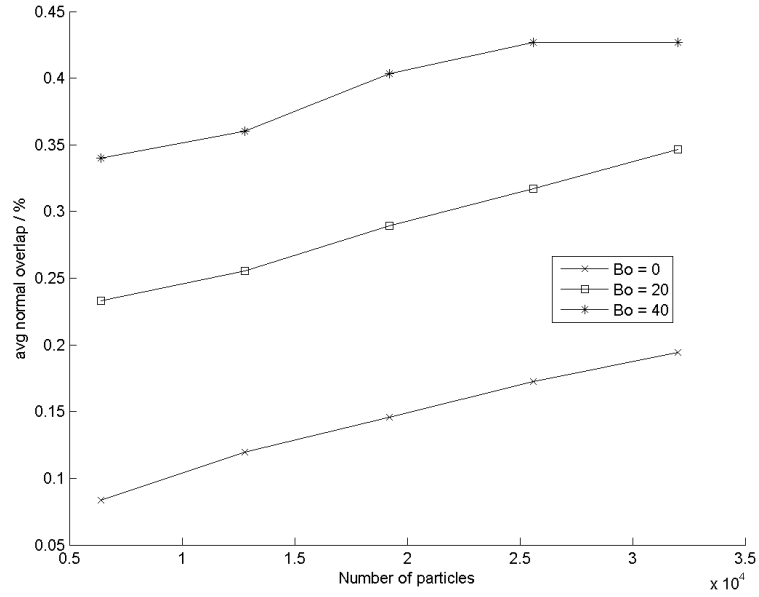
Figure 7: Average normal overlap at different fill heights (geometry 2, 10 rpm, $d_p = 3\,\text{mm}$)
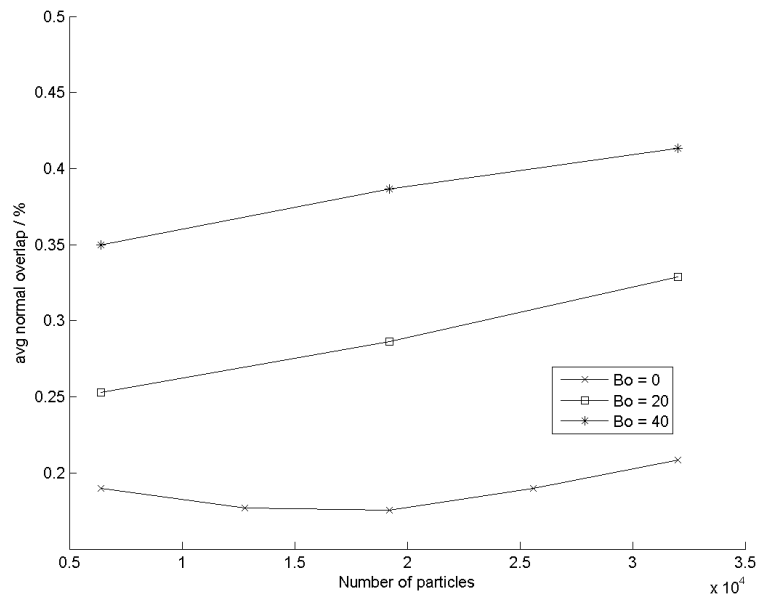
Figure 8: Average normal overlap at different fill heights (geometry 2, 200 rpm, $d_p = 3\,\text{mm}$)

16

2.5 Steady state

To judge whether steady state was reached, the kinetic energy of the particle bed was calculated from the particle masses m_i and the particle speed v_i:

$$E_{kin} = \sum m_i * v_i^2 \tag{43}$$

The system was assumed to be at steady state once the long-term average of the kinetic energy was reached.

2.6 Mixing

To evaluate the mixing in the simulations, the monodisperse particle bed was studied visually. Before the onset of the impeller motion, the particle bed was horizontally divided into two same-sized fractions of particles of different colors. The mixing quality at any given time step could easily be estimated visually. In addition, the relative standard deviation (RSD) of the entire particle bed was determined [19]. To that avail, the simulation domain was divided into a sample grid.

$$\text{RSD} = \frac{\sigma_{\text{conc}}}{M_{\text{conc}}} \tag{44}$$

σ_{conc} was the standard deviation of the particle concentration of one of the particle fractions over all the sample cells and M_{conc} was the overall mean particle concentration, which amounted to $M_{\text{conc}} = 0.5$ for each of the two particle fractions. The RSD of the system is sensitive to the size of the sampling grid [4, p. 447], and typically the size of the sampling grid in pharmaceutical processes is chosen to be the size of the product (e.g. the unit dose) [5, p. 110f]. Brenda Remy [17, p. 43] cited a grid size of about 5 particle diameters for a similar geometry. Within the scope of this work, a cubic grid with a grid size of 10 mm was chosen.

The particle diffusivities were calculated according to equation 45. The time step was set to one blade pass, or $^1/_4$ of a revolution [2] [20].

$$D_{ij} = \left|(\Delta x_i - \bar{\Delta x_i})(\Delta x_j - \bar{\Delta x_j})\right| \frac{1}{2\Delta t} \tag{45}$$

They were then normalized with the tip speed V_{tip} and the tank diameter D:

$$D_{ij}^* = \frac{D_{ij}}{DV_{\text{tip}}} \tag{46}$$

[2]

2.7 Power spectrum

The power spectrum of the shear stress data from the simulations was analyzed. The power spectrum $S_{xx,j}$ of the Signal x at the frequency j was be calculated as

$$S_{xx,j} = 2\frac{\Delta^2}{T}X_j X_j^* \tag{47}$$

In this equation, Δ denotes the sampling interval and T is the duration of the signal recording. X_j is the Fourier transform of x, and X_j^* is its complex conjugate. [9]

The Nyquist frequency, which is half the sampling frequency of the simulation (see equation 48), is the highest frequency that can be observed at a given sampling rate. [9]

$$f_{\text{Nyquist}} = \frac{1}{2\Delta} \tag{48}$$

All simulations were set to a sampling rate of $0.1\,\text{s}^{-1}$, and the resulting Nyquist frequency was $f_{\text{Nyquist}} = 5\,\text{s}^{-1}$.
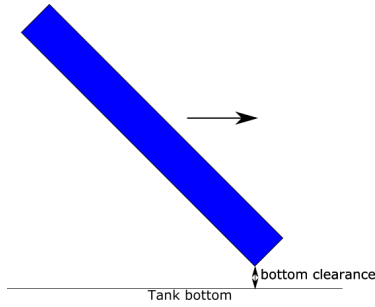
Figure 9: Blade design (a)
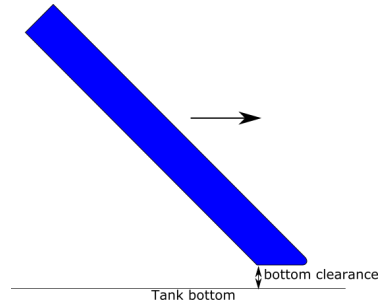
Figure 10: Blade design (b)

3 Effect of the geometry

3.1 Blade shape

Simulations were run at blade clearances reaching from 0.1 mm to 40 mm. For blade clearances significantly higher than the particle diameter, a simple blade design was employed (see blade design a in figure 9). At blade clearances similar to or lower than the particle diameter, this blade design led to very high contact forces between the lower front edge of the blade and the particles. As a result, the overlap became very high and particles started to pass through the vessel wall and leave the simulation.

To avoid these high contact forces, a different blade design was introduced (see design b in figure 10). At low clearances, the blades swept particles from the floor rather than pushing them down. The shape, as well as the rounded edges, led to more stable simulations.

3.2 Wall clearance

A wall clearance similar in value to the particle diameter led to very high overlaps between the blades and the particles and subsequently to high contact forces and particle velocities. To avoid this effect, the ratio of the wall clearance to the particle diameter was either kept higher than two (e.g. 2.5 in the geometry 1) or significantly below one (e.g. 0.67 in the geometry 2).

3.3 Blade clearance

The influence of the distance of the blades from the bottom at a fill level just covering the blades was studied. The friction μ_s of the particles was varied from 0.1 to 1 and the studied range of rotational speeds was 10 rpm to 200 rpm.

At a bottom clearance of 5 mm and a fill level of 30 mm, the whole particle bed was moved by the impeller. This motion caused the particle bed to rise to a height of up to 45 mm as the rotational speed was set to up to 200 rpm.

At a bottom clearance of 40 mm and a fill level of 60 mm, a stagnant region formed at the bottom of the tank. In the quasistatic regime, the stagnant region measured 35 mm of the particle bed regardless of the friction (see figure 11).

19

In the intermediate regime (200 rpm), the fill level rose to 80 mm. The high-friction simulations in that regime still showed a clear distinction between the moved part of the bed and the stagnant region (see figure 12). The simulations with a friction of $\mu_s = 0.1$ on the other hand showed a wider transition zone from the moved bed to the stagnant region (see figure 13).
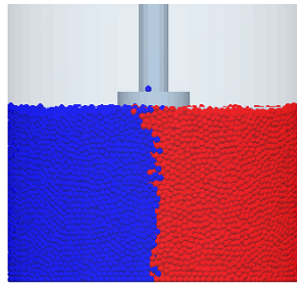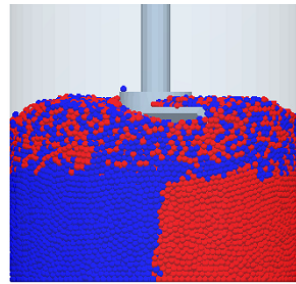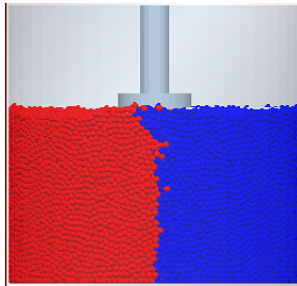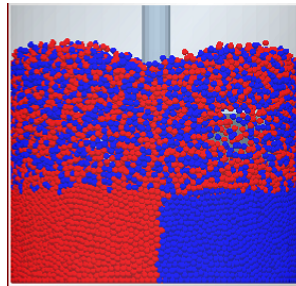
(a) At 0 revolutions (b) At 5 revolutions

Figure 11: Side view of the reactor (40 mm blade clearance, 10 rpm, $\mu_s = 0.1$)

(a) At 0 revolutions (b) At 5 revolutions

Figure 12: Side view of the reactor (40 mm blade clearance, 200 rpm, $\mu_s = 1.0$)
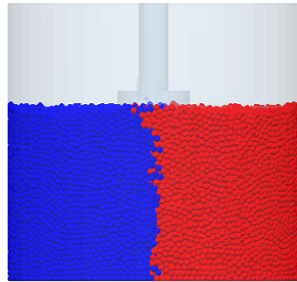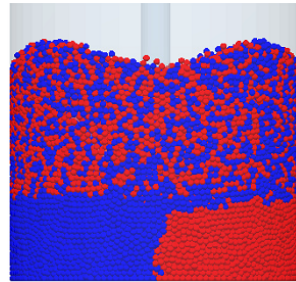
(a) At 0 revolutions (b) At 5 revolutions

Figure 13: Side view of the reactor (40 mm blade clearance, 200 rpm, $\mu_s = 0.1$)
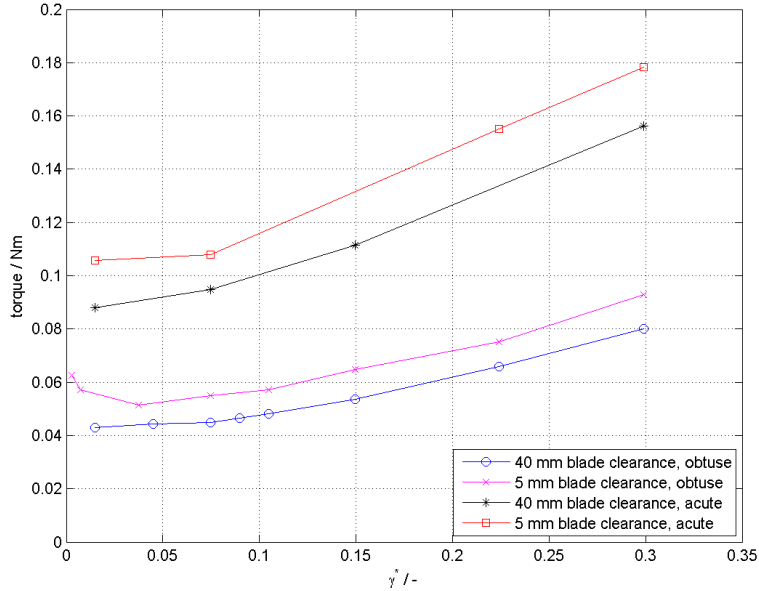
Figure 14: Torque vs dimensionless shear rate at different blade clearances (geometry 1, $\mu_s = 1.0$)

Figure 14 shows the torque over the dimensionless shear rate γ^* for different blade clearances at a static friction of $\mu_s = 1.0$. For both blade orientations - acute and obtuse - the torque was distinctly lower for simulations with a blade clearance of 40 mm than for those with a clearance of 5 mm. The low blade clearance led to a high shear rate in the thin particle layer below the blade, which resulted in a high torque on the impeller.

3.4 Blade orientation

As can be seen in figure 14, the torque exerted on the impeller was approximately twice as high in the case of the acute blade orientation than with the obtuse orientation. This correlated with the pressure exerted on the tank bottom by the blades (see table 1). It changed only little with the rotational speed but was dependent on the blade clearance and the blade orientation. The pressure more than doubled in the geometry with a blade clearance of 5 mm when the blade orientation was switched from obtuse to acute, while in the 40 mm case it only increased by roughly 50 %. It is assumed that the larger blade clearance in the latter case led to more load being taken by the walls instead of the bottom of the tank.

3.5 Fill level

The geometry 2 simulations were studied at different fill levels (number of particles ranging from 6400 to 32 000, fill level 30 mm to 122 mm) with and without

	5 mm blade clearance	40 mm blade clearance
obtuse	357 Pa	766 Pa
acute	795 Pa	1126 Pa

Table 1: Average pressure at tank bottom, geometry 1 ($\mu_s = 1.0$, 200 rpm)

cohesive forces (i.e., with and without liquid). The resulting torque values for the dry simulations can be seen in figure 17.

Figure 15 shows the increase in impeller torque as the fill level increases in the quasistatic regime ($\gamma^* = .018$) for the geometry 2. Figure 16 shows the same relation in the intermediate regime ($\gamma^* = 0.366$).

The increase in pressure at higher fill heights resulted in higher torque fluctuations. Figure 18 shows the torque fluctuation $T' = T - \bar{T}$ for different fill heights at 10 rpm. The increase in the standard deviation of T' with the fill height is shown in figure 19.

An analysis of the normal stress showed that the profiles of the normal stress P over the height of the bed were similar for the dry and the wet simulations. The normal stress curves were compared to the hydrostatic pressure, which in turn was obtained from the bulk density profiles:

$$P_{hyd}(h_i) = \int_{h_i}^{H} \rho_{bulk}(h) \, g \, dh \tag{49}$$

In the region above the blades, the hydrostatic pressure calculation was able to approximate the normal stress (see figure 20). In the blade region, the normal stress was lower than the hydrostatic prediction for all different fill heights. This decrease was observed in all three individual components of the normal stress (see figure 21).
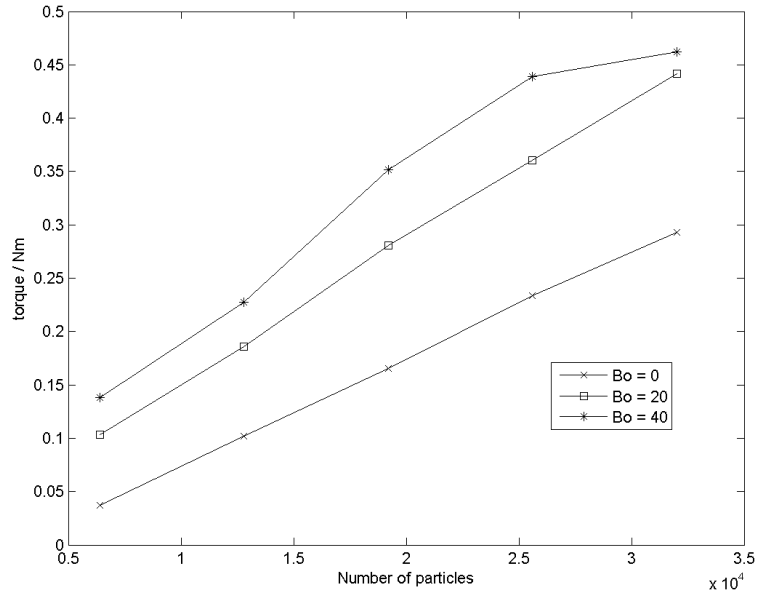
Figure 15: Torque vs number of particles at 10 rpm (blade clearance 0.1 mm, geometry 2)
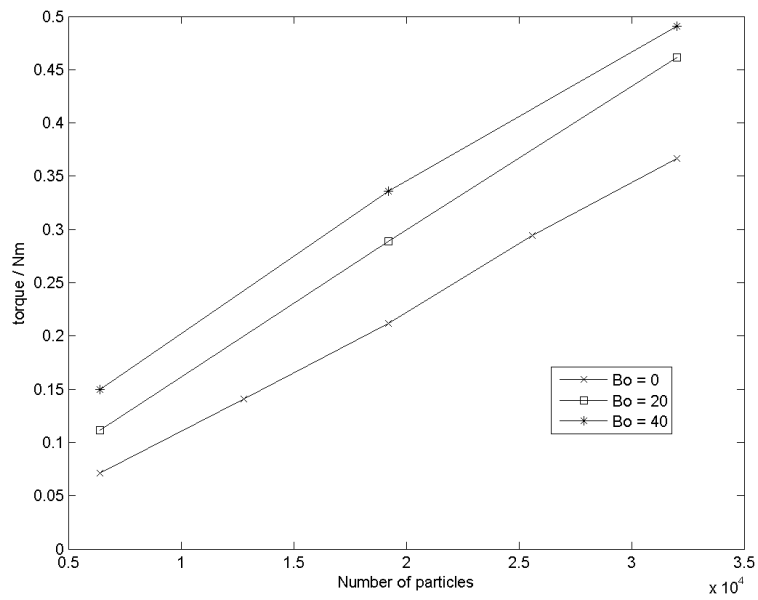

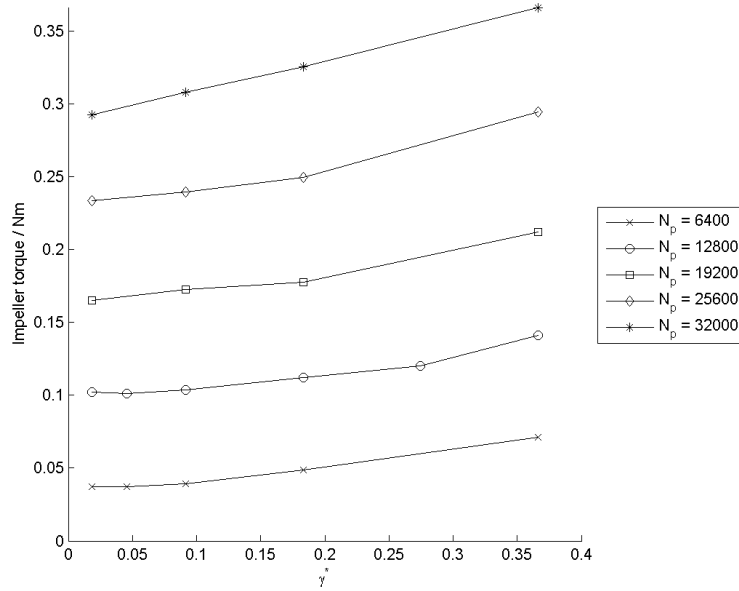Figure 16: Torque vs number of particles at 200 rpm (Blade clearance 0.1 mm, geometry 2)

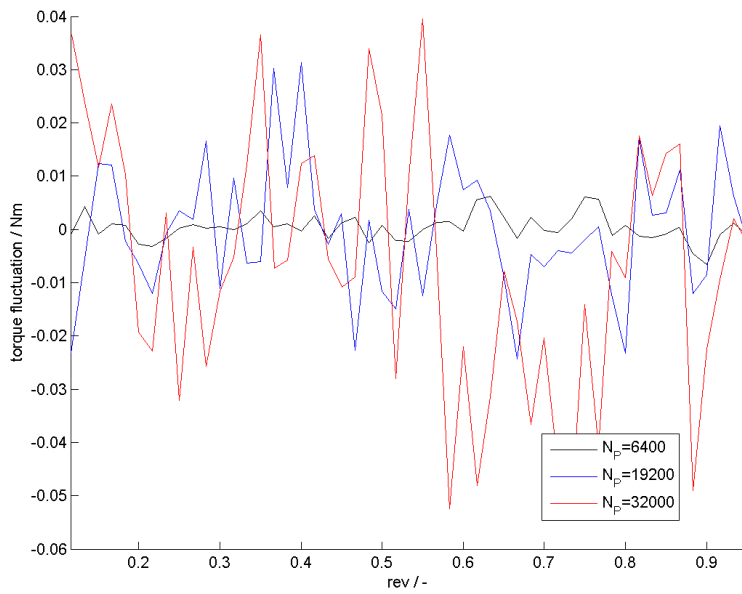Figure 17: Torque vs γ^* at different fill levels in the geometry 2 ($\mu_s = 0.5$, $Bo = 0$)

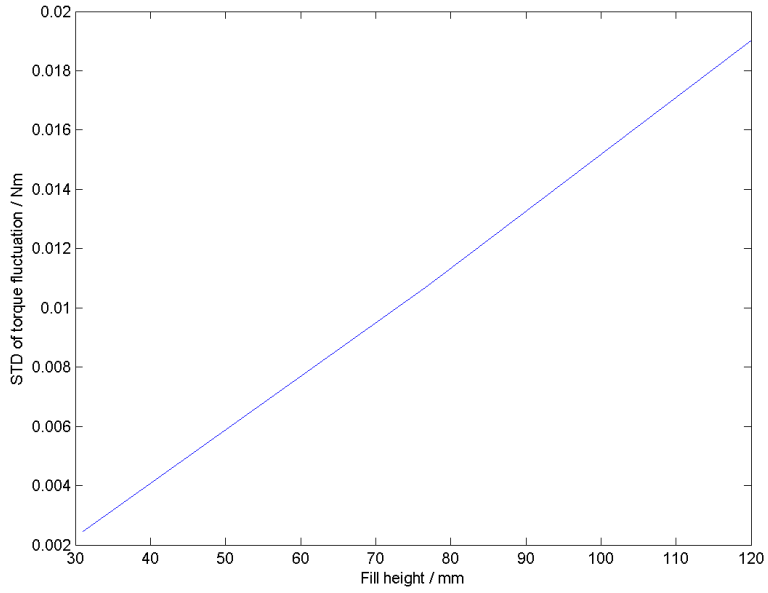Figure 18: Torque fluctuation at different fill heights (geometry 2, 10 rpm, $\mu_s = 0.5$, geometry 2, $Bo = 0$)

Figure 19: Standard deviation of $(T - \bar{T})$ vs fill height (geometry 2, 10 rpm, $\mu_s = 0.5$, geometry 2, $Bo = 0$)
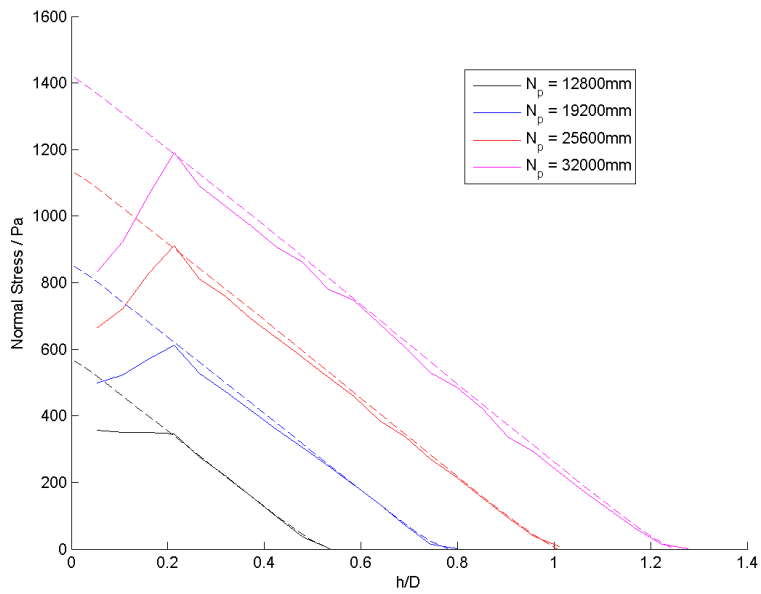
Figure 20: Normal stress (solid lines) and hydrostatic pressure (dashed lines) at different fill heights (geometry 2, $Bo = 0$, 10 rpm)
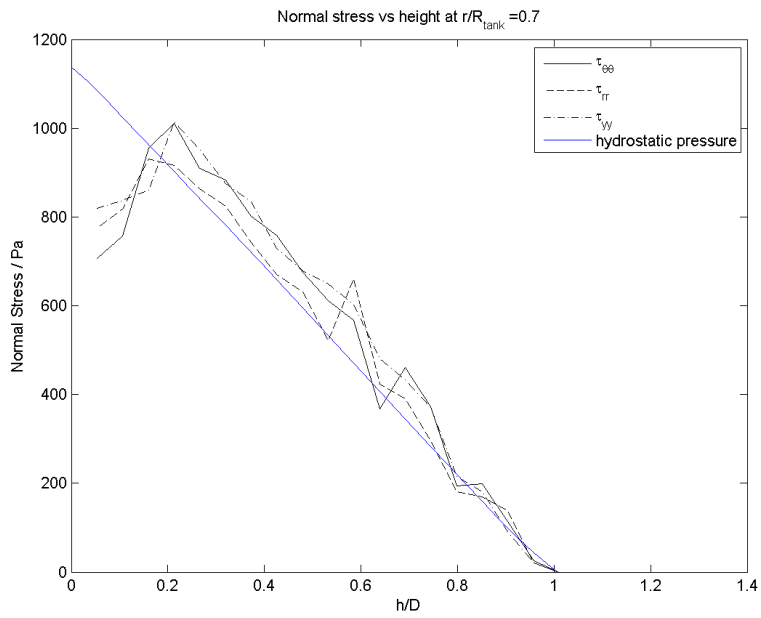
Figure 21: Individual normal stress components and hydrostatic pressure at $H/D = 1$ (geometry 2, $Bo = 0$, 10 rpm)

4   Effect of the static friction

The static friction coefficient μ_s was varied between 0.1, 0.5 and 1 and was always set to identical values for the particle-particle and the particle-wall interaction.

A study [18] that used shear cell analyses to experimentally determine the friction of glass beads reported a friction of $\mu_s = 0.32$ for uncoated glass beads. It was further shown that a static friction of $\mu_s = 0.5$ in the DEM simulation of a similar geometry provided comparable results. A different study [7] reported the friction of spherical glass beads at diameters of $1\,\mu m$ to $800\,\mu m$ in a shear cell to be in the range of 0.44 to 0.47.

Another study [24] showed that sliding frictions of both 0.3 and 0.5 yielded good results for the simulations of a bladed vertical tank mixer when compared to experiments. Increasing the friction from $\mu_s = 0.2$ to 0.3 had a significant effect on the simulation while the change of the velocity profile was less pronounced between values of 0.3 and 0.5.

Figure 22 shows the speed profile of the particles in the geometry 1 at 50 rpm and 5 mm blade clearance. The simulation with a high static friction coefficient ($\mu_s = 1.0$) yielded a speed distribution profile that was shifted towards slower speeds compared to the one predicted by the rigid bed theory. A reduction of the coefficient of friction by one order of magnitude led to a speed profile that was close to that of the ideal rigid bed. The same effect was observed by Stewart [24]. At low frictions, the particles tended to move as one block, while at higher frictions they were significantly slowed down by the walls and the tank bottom. This observation held true for the whole simulated rpm range of 10 rpm to 200 rpm. This led to faster mixing at higher frictions (see figure 23). It is noteworthy that the difference between a friction coefficient of 0.1 and 0.5 was more pronounced than the difference between 0.5 and 1.0.

The impeller torque increased at higher μ_s (see figure 24). At very low rotational speeds (down to 1 rpm), the torque started to rise with decreasing speed. This behavior is indicative of the stick-slip regime and was especially pronounced in high friction simulations.
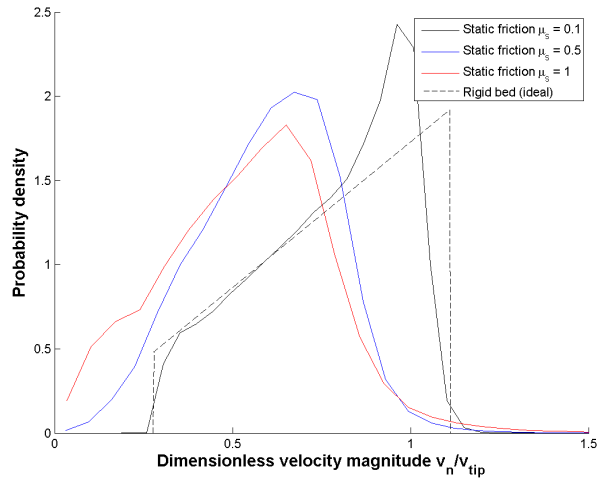
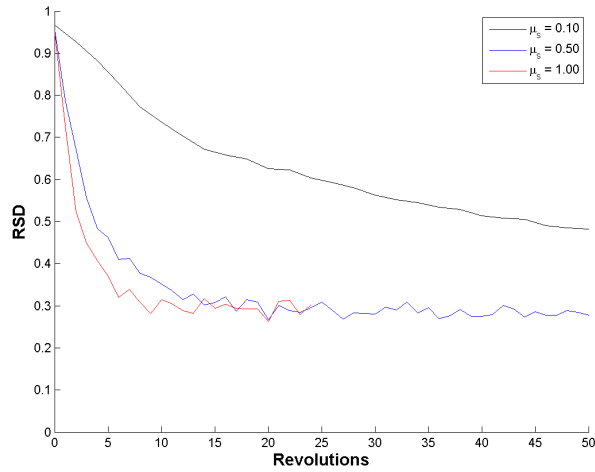Figure 22: Speed profiles at different values for the static friction μ_s in the geometry 1 at 50 rpm and with $5\,\mathrm{mm}$ blade clearance

Figure 23: RSD over revolutions for geometry 1 simulations (50 rpm, obtuse blade orientation, $G = 8.6 \times 10^6\,\mathrm{Pa}$) at different frictions μ_s
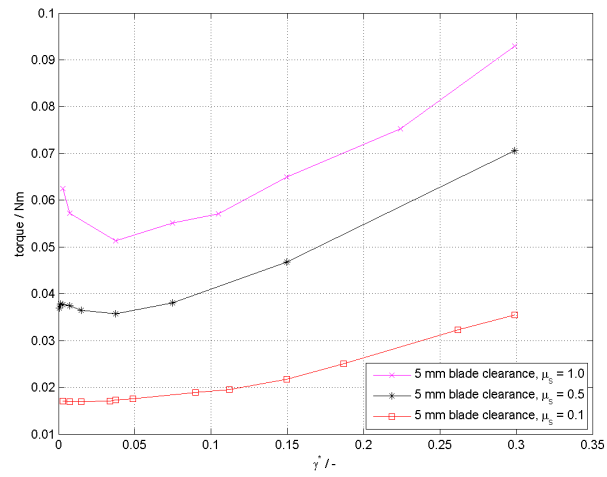
29

Figure 24: Torque vs γ^* for the geometry 1 at 50 rpm and 5 mm blade clearance at different frictions

5 Effect of cohesiveness

The dimensionless liquid bridge volume $\hat{V}$, the surface tension γ of the liquid and the liquid wetting angle θ were set as parameters for the cohesion model. While the liquid bridge volume $\hat{V} = 0.04$ and the wetting angle $\theta = 0$ were left unchanged in the scope of this work, the surface tension γ was varied to change the cohesiveness of the system.

The Bond number of the system was then evaluated using the relation suggested by Li et al. [10] (see section 1.3.3).

Simulations were run at Bond numbers ranging from 0 (dry system) to 40. The coefficient of friction was left at $\mu_s = 0.5$ for all the simulations.

Figure 25 shows the torque for the dry and wet simulations at a fill height that just covered the blades. These simulations showed quasistatic regimes as predicted by Tardos (see section 1.2), although the quasistatic regime was less pronounced at $Bo = 0$ than at higher Bond numbers. Figure 26 shows the effect of increasing the fill level drastically. The dry simulations at high fill level did not have a distinct quasistatic regime in the studied rpm range. In the wet simulations, on the other hand, The torque even started to rise sharply as the shear rate was reduced at the high fill level.

Figure 27 shows the increase of the torque with the Bond number for different fill heights.

The mixing of quasistatic particle beds that are just covering the blades is shown in figure 28 and 29. It can be noted that the best mixing occurred in the simulation with the highest Bond number. Furthermore, the particle bed lagged behind the blades in all the simulations, i.e. the bed did not rotate as fast as the blades.

Showing the RSD value over time allowed for a quantitative analysis of the mixing behavior (see figure 30). Simulations with high Bond numbers demonstrated a high initial mixing rate, while low Bond numbers correlated with slow initial mixing. After a few revolutions, the simulations with high Bond numbers were mixing slower than those with low Bond numbers.

Figure 31 shows how the diffusivity changed for the studied quasistatic simulations as the Bond number increased. Similar to Remy's observations [20], the diffusivity increased initially as the Bond number was increased, before decreasing again at very high Bond numbers.

In the range of the blades, the power spectrum of the shear stress showed a dominant frequency of around four times the rotational speed of the impeller, independent of the fill height and the Bond number. This frequency is equivalent to the frequency of blade passes of the four-bladed impeller. The second dominant frequency was at eight times the impeller frequency, i.e. twice the blade pass frequency.
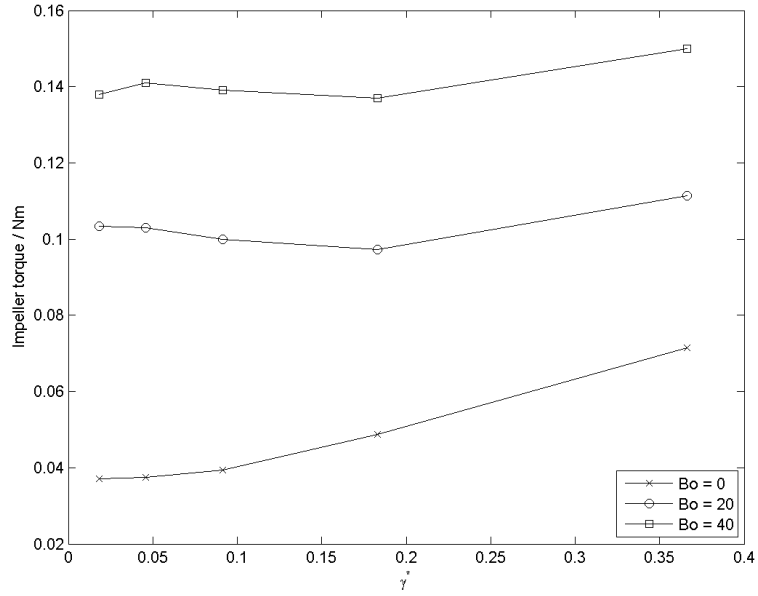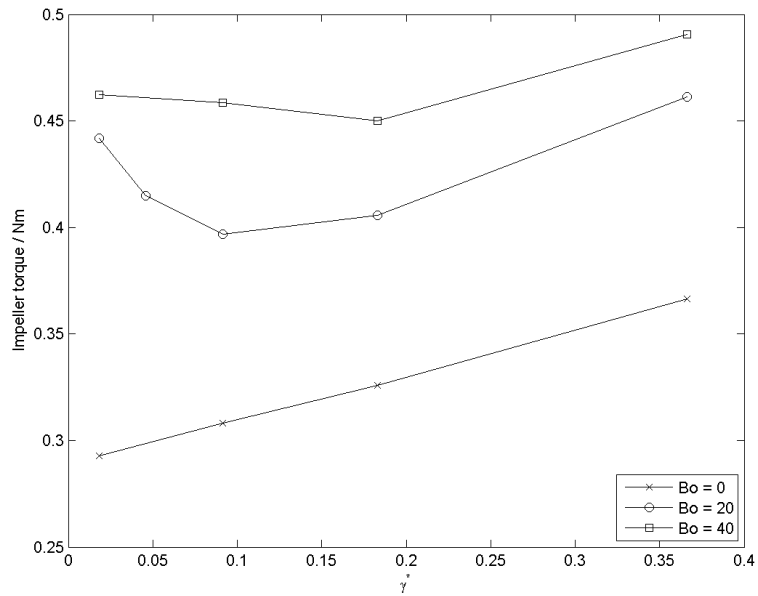
Figure 25: Torque vs γ^* (geometry 2, $N_p = 6400$)

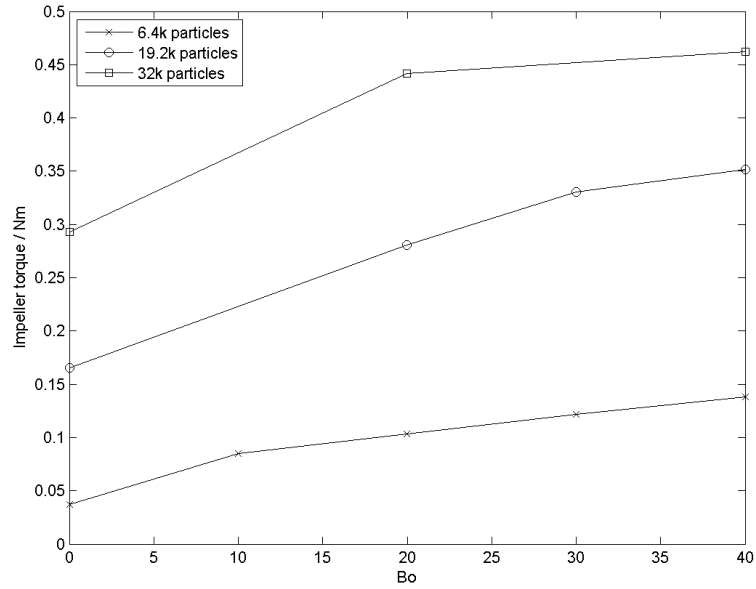Figure 26: Torque vs γ^* (geometry 2, $N_p = 32000$)

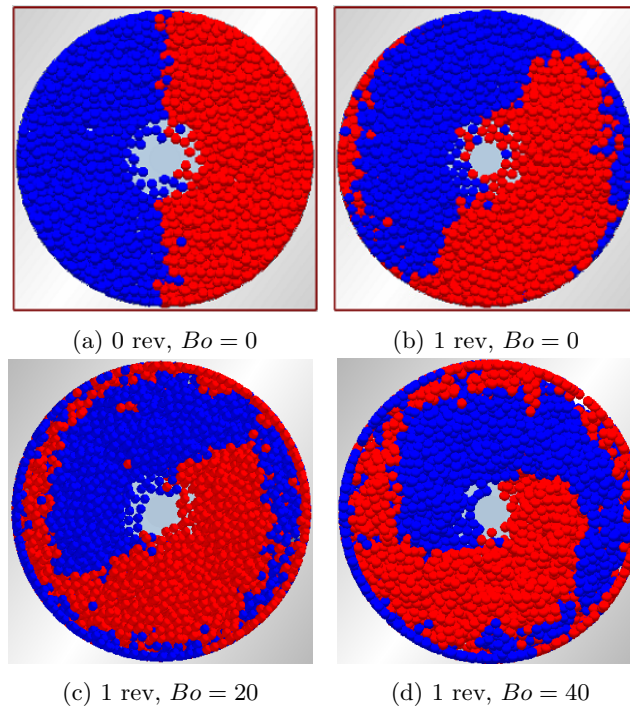Figure 27: Torque vs Bond number at different fill heights (geometry 2, 10 rpm)

(a) 0 rev, $Bo = 0$

(b) 1 rev, $Bo = 0$

(c) 1 rev, $Bo = 20$

(d) 1 rev, $Bo = 40$

Figure 28: Top view of the reactor (geometry 2, 10 rpm), $N_p = 6400$

(a) 0 rev, $Bo = 0$ (b) 1 rev, $Bo = 0$
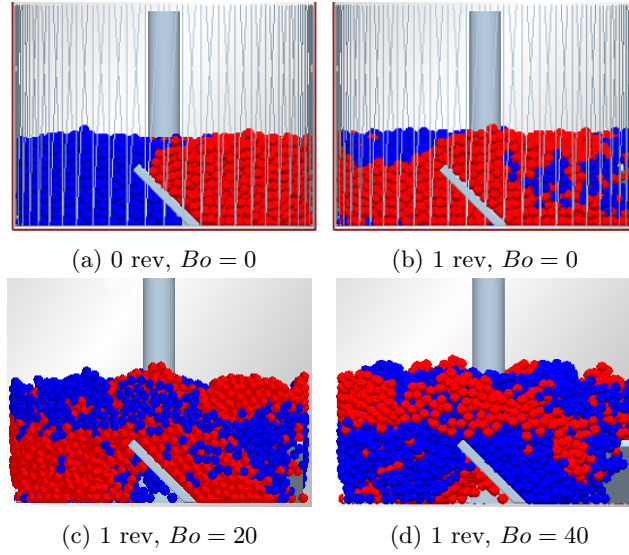
(c) 1 rev, $Bo = 20$ (d) 1 rev, $Bo = 40$

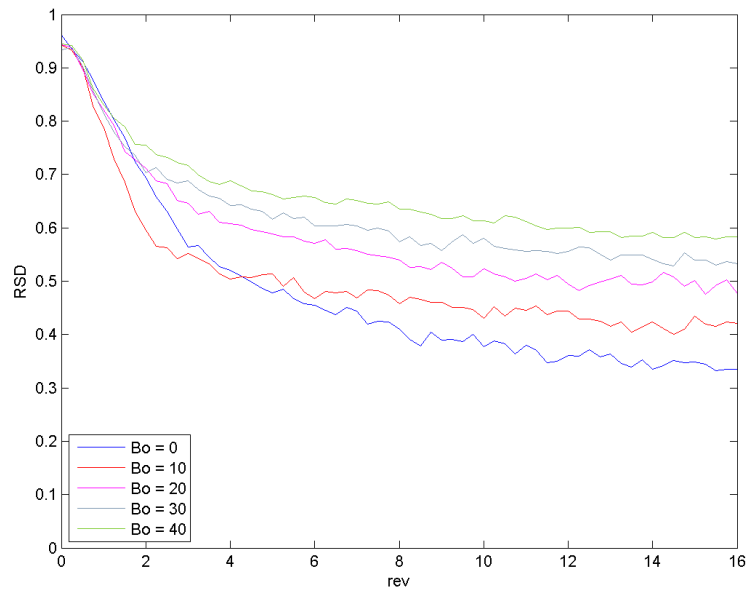Figure 29: Side view of the reactor (geometry 2, 10 rpm, $N_p = 6400$)

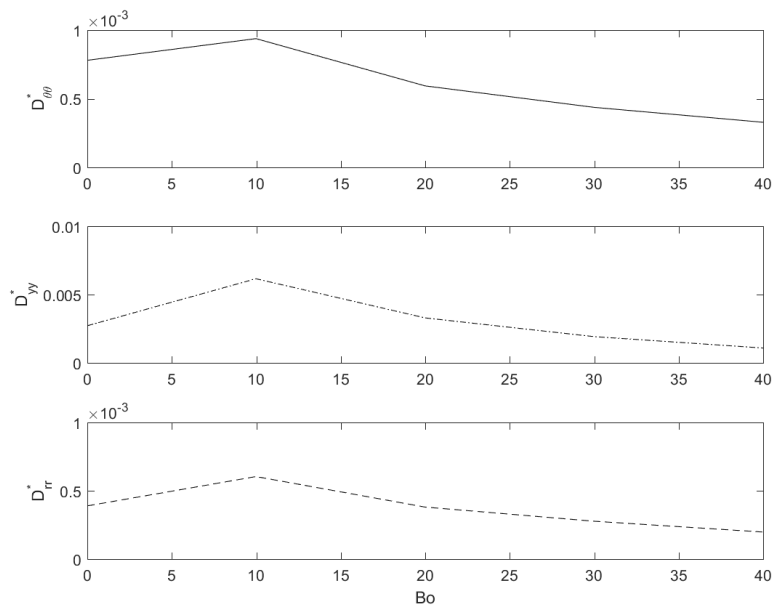Figure 30: RSD vs revolutions at different Bo numbers

Figure 31: Dimensionless diffusivity D^* vs Bond number (geometry 2, $N_p = 6400$, 10 rpm)

A   Appendix

A.1   Geometry

The dimensions of the simulated mixers are listed in table 2 and table 3.

A.2   Simulation parameters

Table 4 shows the input parameters for the particles in the simulations.

Dimension	Value
Tank diameter D	100 mm
Shaft diameter D_{shaft}	25 mm
Blade diameter D_{blade}	90 mm
Height of blades h_{blade}	19.2 mm
Blade clearance from bottom	0.1 mm to 40 mm
Particle diameter d_p	2 mm

Dimensionless geometry number	Value
Tank diameter/particle size	50
Blade diameter/tank diameter	0.9
Blade clearance/particle diameter	2.5 to 20
Wall clearance/particle diameter	2.5

Table 2: Dimensions of the geometry 1

Dimension	Value
Tank diameter D	94 mm
Shaft diameter D_{shaft}	25 mm
Blade diameter D_{blade}	90 mm
Height of blades h_{blade}	19.2 mm
Blade clearance from bottom	0.1 mm to 1 mm
Particle diameter d_p	3 mm

Dimensionless geometry number	Value
Tank diameter/particle size	31.3
Blade diameter/tank diameter	0.9
Blade clearance/particle diameter	0.033 to 0.333
Wall clearance/particle diameter	0.667

Table 3: Dimensions of the geometry 2

Variable	Symbol	Value
Rolling friction coefficient	μ_r	0.005
Static friction coefficient	μ_s	0.1 to 0.5
Particle density	ρ	$2.2\,\text{g}\,\text{l}^{-1}$
Shear modulus	G	$2.6 \times 10^6\,\text{Pa}$ to $2.6 \times 10^{10}\,\text{Pa}$
Coefficient of restitution	e	0.6
Poisson's ratio	ν	0.25

Table 4: Simulation parameters

Acknowledgements

References

[1] Anshu Anand, Jennifer S. Curtis, Carl R. Wassgren, Bruno C. Hancock, and William R. Ketterhagen. Predicting discharge dynamics of wet cohesive particles from a rectangular hopper using the discrete element method (dem). *Chemical Engineering Science*, 64(24):5268 – 5275, 2009.

[2] Charles S. Campbell. Self-diffusion in granular shear flows. *Journal of Fluid Mechanics*, 348:85–101, 10 1997.

[3] Charles S. Campbell. Granular material flows – an overview. *Powder Technology*, 162(3):208 – 229, 2006.

[4] R. P. Chhabra. *Non-Newtonian Flow and Applied Rheology Engineering Applications*. Elsevier Science, City, 2011.

[5] P. J. Cullen. *Pharmaceutical blending and mixing*. Wiley, Chichester, Sussex, UK Hoboken, NJ, 2015.

[6] Mindlin R. D. Compliance of elastic bodies in contact. *J Appl Mech.*, 16:259 – 268, 1949.

[7] Kevin M. Frye and Chris Marone. The effect of particle dimensionality on granular friction in laboratory shear zones. *Geophysical Research Letters*, 29(19):22–1–22–4, 2002. 1916.

[8] K. Hutter and K.R. Rajagopal. On flows of granular materials. *Continuum Mechanics and Thermodynamics*, 6(2):81–139, 1994.

[9] Mark A. Kramer. An introduction to field analysis techniques: The power spectrum and coherence, 2013.

[10] Hongming Li and J. J. McCarthy. Controlling cohesive particle mixing and segregation. *Phys. Rev. Lett.*, 90:184301, May 2003.

[11] Guoping Lian, Colin Thornton, and Michael J. Adams. A theoretical study of the liquid bridge forces between two rigid spherical bodies. *Journal of Colloid and Interface Science*, 161(1):138 – 147, 1993.

[12] Stef Lommen, Dingena Schott, and Gabriel Lodewijks. {DEM} speedup: Stiffness effects on behavior of bulk material. *Particuology*, 12:107 – 112, 2014. Special issue on conveying and handling of particulate solids – Challenges of discrete element simulation, application and calibration.

[13] Kevin Francis Malone and Bao Hua Xu. Determination of contact parameters for discrete element method simulations of granular systems. *Particuology*, 6(6):521 – 528, 2008. Simulation and Modeling of Particulate Systems.

[14] Roman Mani, Dirk Kadau, and Hans J. Herrmann. Liquid migration in sheared unsaturated granular media. *Granular Matter*, 15(4):447–454, 2013.

[15] Takafumi Mikami, Hidehiro Kamiya, and Masayuki Horio. Numerical simulation of cohesive powder behavior in a fluidized bed. *Chemical Engineering Science*, 53(10):1927 – 1940, 1998.

[16] Namiko Mitarai and Franco Nori. Wet granular materials. *Advances in Physics*, Februar 2006.

[17] Brenda Remy. *Granular Flow, Segregation and Agglomeration in Bladed Mixers*. PhD thesis, Rutgers, The State University of New Jersey, October 2010.

[18] Brenda Remy, Thomas M. Canty, Johannes G. Khinast, and Benjamin J. Glasser. Experiments and simulations of cohesionless particles with varying roughness in a bladed mixer. *Chemical Engineering Science*, 65(16):4557 – 4571, 2010.

[19] Brenda Remy, Johannes G. Khinast, and Benjamin J. Glasser. Discrete element simulation of free flowing grains in a four-bladed mixer. *AIChE Journal*, 55(8):2035–2048, 2009.

[20] Brenda Remy, Johannes G. Khinast, and Benjamin J. Glasser. Wet granular flows in a bladed mixer: Experiments and simulations of monodisperse spheres. *AIChE Journal*, 58(11):3354–3369, 2012.

[21] DEM Solutions. Edem 2.6. Computer Program (Source Code).

[22] DEM Solutions. *EDEM 2.6 User Guide*. DEM Solutions.

[23] DEM Solutions. *EDEM Contact Model: Hertz-Mindlin with Liquid Bridge*. DEM Solutions.

[24] R.L. Stewart, J. Bridgwater, Y.C. Zhou, and A.B. Yu. Simulated and measured flow of granules in a bladed mixer—a detailed comparison. *Chemical Engineering Science*, 56(19):5457 – 5471, 2001. Festschrift in honour of Dr. R.A. Mashelkar.

[25] Gabriel I. Tardos, Sean McNamara, and Ilkay Talu. Slow and intermediate flow of a frictional bulk powder in the couette geometry. *Powder Technology*, 131(1):23 – 39, 2003.

[26] Y. Tsuji, T. Tanaka, and T. Ishida. Lagrangian numerical simulation of plug flow of cohesionless particles in a horizontal pipe. *Powder Technology*, 71(3):239 – 250, 1992.

[27] RY Yang, RP Zou, and AB Yu. Numerical study of the packing of wet coarse uniform spheres. *AIChE journal*, 49(7):1656–1666, 2003.